# Lawrence Berkeley National Laboratory

**Title**
Dissolution-Assisted Pattern Formation During Olivine Carbonation

**Authors**
Lisabeth, Harrison
Zhu, Wenlu
Xing, Tiange
et al.

# Dissolution-Assisted Pattern Formation During Olivine Carbonation

Harrison Lisabeth[1,2], Wenlu Zhu[1], Tiange Xing[1], Vincent De Andrade[3]

1 Department of Geology, University of Maryland, College Park, MD, USA, 2 Department of Geophysics, Stanford University, Stanford, CA, USA, 3 Advanced Photon Source, Argonne National Laboratory, Lemont, IL, USA

## Abstract

Olivine and pyroxene-bearing rocks in the oceanic crust react with hydrothermal fluids producing changes in the physical characteristics and behaviors of the altered rocks. Notably, these reactions tend to increase solid volume, reducing pore volume, permeability, and available reactive surface area, yet entirely hydrated and/or carbonated rocks are commonly observed in the field. We investigate the evolution of porosity and permeability of fractured dunites reacted with $CO_2$-rich solutions in laboratory experiments. The alteration of crack surfaces changes the mechanical and transport properties of the bulk samples. Analysis of three-dimensional microstructural data shows that although precipitation of secondary minerals causes the total porosity of the sample to decrease, an interconnected network of porosity is maintained through channelized dissolution and coupled carbonate precipitation. The observed microstructure appears to be the result of chemo-mechanical coupling, which may provide a mechanism of porosity maintenance without the need to invoke reaction-driven cracking.
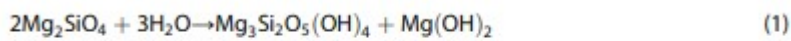
## Plain Language Summary

When carbon dioxide reacts with certain minerals, it can be transformed into solid carbonate minerals. These carbonate minerals can be deposited at the site of the interaction between the fluid and the solid. It is often assumed that the armoring of surfaces by the products of such a reaction will shut down the reaction in a self-limiting fashion. However, rocks that are the result of the complete conversion of reactive minerals to carbonate and other minerals via interaction with carbon dioxide are observed in nature. This paper presents the results of experiments designed to constrain the mechanism allowing such reactions to proceed to completion. We find that a coupled dissolution-precipitation process results in the formation of a system of channels in the rock that allow continuous fluid access to solid surfaces. This result is essential for the complete understanding of fluid-rock interactions in natural systems and may be important to consider when modeling geological carbon storage by mineral carbonation.

## 1 Introduction

Hydration and carbonation of ultramafic rocks are widespread processes on the surface of the Earth. Along mid-ocean ridges or at subduction zones, the olivine and pyroxene-bearing rocks in the oceanic crust react with hydrothermal fluids to produce minerals such as serpentine, brucite, talc, magnesite, and calcite (Deschamps et al., 2013). These volatilization

reactions cause vast physical and chemical changes in the geological systems that host them and their impacts on the Earth system are far reaching, from oceanic tectonics (Escartin et al., 1997) to hydrothermal ecosystems (Kelley et al., 2005). These reactions are exothermic and can proceed vigorously and irreversibly. Where ultramafic rocks have been tectonically juxtaposed against metamorphosed carbonate-bearing sediments, olivine and pyroxene can be entirely converted to carbonate and quartz (Beinlich et al., 2012; Falk & Kelemen, 2015). As such, they have been suggested as a reservoir for long-term geological carbon sequestration (Seifritz, 1990; Kelemen & Matter, 2008). Yet the mechanism that allows these positive volume-changing reactions to proceed to completion is not fully understood.

Volatilization reactions generally involve an increase in solid volume. Simple examples of the hydration and carbonation of forsterite such as

$$2Mg_2SiO_4 + 3H_2O \rightarrow Mg_3Si_2O_5(OH)_4 + Mg(OH)_2 \qquad (1)$$

$$Mg_2SiO_4 + 2CO_2 \rightarrow 2MgCO_3 + SiO_2 \qquad (2)$$

for instance, result in solid volume changes of 46% and 88%, respectively. These reactions require a sufficient supply of fluid reactants to be available within the pore space of the host rocks. The conventional wisdom is that such volume increasing fluid-rock interactions are self-limiting, unless the reactants are precipitated outside of the host rock. However, in nature, it is common to observe entirely hydrated and/or carbonated peridotite, even in isochemical systems (Kelemen & Matter, 2008). Reaction-driven cracking via force of crystallization is often invoked to explain the maintenance of porosity and permeability during fluid-rock reactions that increases the solid volume (Jamtveit et al., 2008; Kelemen & Hirth, 2012; Plumper et al., 2012). While crystallization pressure-induced fracturing is well known at unconfined conditions, such as salt crystallization producing fractures in cement, asphalt, or structural stone (e.g., Scherer, 2004), experimental evidence for reaction-driven cracking under subsurface confinement is sparse. Confined reaction-driven cracking has been observed in engineered materials (Wolterbeek et al., 2016), and some recent experiments have shown that extensional cracks can be formed under confinement by nonuniform volumetric expansion due to precipitation in porous materials (Zhu et al., 2016); however, previous studies have also shown limiting behaviors such as passivation and pore clogging before observing fracturing (e.g., Andreani et al., 2009; Hövelmann et al., 2012). The nonuniform observation of conventional reaction-driven cracking during olivine hydration and carbonation experiments suggests the existence of an alternative mechanism for the maintenance of porosity and permeability in an actively volatilizing system that does not require conventional brittle fracturing.

Insight on the mechanism of fluid ingress into hydrating and carbonating rocks can be gained by looking at the resultant rock structures on the grain

to outcrop scale. Common hallmarks of these reactions are hierarchical fracture networks (Iyer et al., 2008; Røyne et al., 2008), mesh textures (Rumori et al., 2004), and layered veins (Andreani et al., 2007). A unifying characteristic of the rock structures is the regular geometric features that occur on multiple scales: similar vein and fracture angles in the case of hierarchical fractures and mesh textures and evenly spaced layering in the case of vein textures. This sort of pattern formation is typical of systems exhibiting local intensification (positive feedback) and lateral inhibition (negative feedback) (Jamtveit & Hammer, 2012). The question remains as to which mechanisms are responsible for these feedbacks in volatilizing ultramafic rocks.

## 2 Experimental Procedure

The material used for these experiments is Twin Sisters dunite, a nearly monomineralic dunite with minor chromite and diopside. The average grain size is ~2 mm. The composition of the constituent olivine is $Fo_{90}$. Right cylinders 1.84 cm in diameter and 3.81 cm long were cored and ground out of dunite slabs. Initial porosity was <<1%, and initial permeability was $<10^{-18}$ $m^2$, so samples were thermally cracked to induce sufficient permeability for experiments.

Thermal cracking was accomplished by heating and rapidly cooling samples in a gas mixing tube furnace. Samples were put in a $CO$-$CO_2$ atmosphere to control oxygen fugacity and prevent oxidation during the heat treatment, brought to 1250°C for 2 h then cooled in <6 h. After thermal cracking, samples were measured on a bench top nitrogen permeameter and helium porosimeter. The average sample porosity after thermal cracking was ~1%, and the average permeability was $10^{-15}$ $m^2$ with a range from $0.7 \times 10^{-15}$ $m^2$ to $1.3 \times 10^{-15}$ $m^2$. Samples were jacketed with thin (127 µm) copper foil and affixed with wire strain gages with a resolution of $10^{-6}$ prior to experiments.

$CO_2$-rich bicarbonate solution was prepared in an external mixing vessel prior to experiments. A schematic of the fluid mixing system and pressure vessel is presented in supporting information Figure S1. The solution was prepared by dissolving $NaHCO_3$ to a concentration of 0.6 M in distilled water. This solution was put into a bolted closure reactor, the headspace purged, and the $CO_2$ introduced to the vessel and pressurized to 3 MPa at room temperature. The vessel was allowed to equilibrate for at least 48 h before the fluid was flushed through the sample. The pH and $pCO_2$ at experimental conditions were calculated using GEOPIG (Johnson et al., 1992) to be 8 and 0.8 MPa, respectively. The pH of distilled water at 150°C is 5.8.

To investigate the effect of chemically reactive fluids on the deformation and microstructural evolution of ultramafic rocks, we perform hydrostatic compaction experiments on thermally cracked dunites saturated with distilled water or a $CO_2$-rich bicarbonate solution. Sample volume change and permeability are monitored in situ throughout 3 days of reaction at 15 MPa confining pressure, 10 MPa pore pressure, and 150°C. One control

experiment was conducted with distilled water at room temperature. Samples are loaded into the triaxial deformation apparatus saturated with distilled water, the pore fluid system purged of bubbles, then brought to experimental conditions. The heating process takes ~8 h to achieve thermal stability. Once at conditions, the samples' pore fluid is flushed with the designated fluid composition for a given experiment, either distilled water or $CO_2$-rich bicarbonate solution. Samples are allowed to react and compact for 3 days, while their strain is constantly monitored and permeability is spot checked. Permeability is measured using pore pressure transient analysis (Boitnott, 1997). At the conclusion of 3 days of reaction, samples are deformed axially until failure to assess the change in their mechanical behavior. A nominal strain rate of $10^{-5}$ $s^{-1}$ is used. Sample stress, strain, and permeability are measured throughout deformation. At the conclusion of tests, samples are cooled, depressurized, and prepared for microstructural analysis.

Samples were cut into several pieces and prepared for several methods of microanalysis. Part of each sample was epoxy impregnated, bisected axially, and made into a traditional-polished thin section. These thin sections were inspected using an optical microscope and regions of interest identified. The thin sections were imaged using a scanning electron microscope (SEM) and spot chemical analyses performed using energy dispersive spectroscopy (EDS). SEM analyses of doubly polished thin sections were performed on a JEOL JXA 8900R Microprobe at 15 kV accelerating voltage. Unpolished portions of the samples were also analyzed to prevent damage to soft reaction products. Samples were broken along preexisting crack surfaces to look at the area most exposed to fluid-rock interaction. Focused ion beam (FIB) sections were cut into the crack face to examine the depth of penetration of fluids (for schematic illustration, see supporting information Figure S2). Spot chemical analyses were performed using EDS to determine mineralogy of phases. Backscattering electron images and qualitative elemental analyses of unpolished samples were performed on a Zeiss Auriga FIB-SEM between 3 and 15 kV accelerating voltage with a beam current of 2–20 nA.

## 3 Results

### 3.1 Mechanical Behavior During Reaction

Mechanical behaviors of samples deformed with different pore fluids point to chemo-mechanical coupling. In the absence of any reaction, the sample with distilled water that deformed at room temperature shows negligible compaction (cyan curve, Figure 1a). The sample with $CO_2$-rich bicarbonate solution at 150°C shows similar behavior to the distilled water sample at the beginning of tests, with a decreasing compaction rate; however, after ~36 h, the compaction rate begins to increase (red curve, Figure 1a). The compaction is initially less in the sample with $CO_2$-rich bicarbonate solution compared to the distilled water sample, but the late-stage increase in

compaction results in higher total compaction by the end of the hydrostatic portion of the experiment. Samples reacted at elevated temperature have lower shear strength than samples reacted at room temperature (Figure 1b). All samples exhibit reduced permeability during hydrostatic compaction (Figure 1c). Complimentary analysis of the effect of this reaction on the mechanical behavior of dunites shows that the reaction leads to a reduction in both strength and Young's modulus and that the effect is sensitive to the pore fluid bicarbonate concentration (Lisabeth et al., 2017).
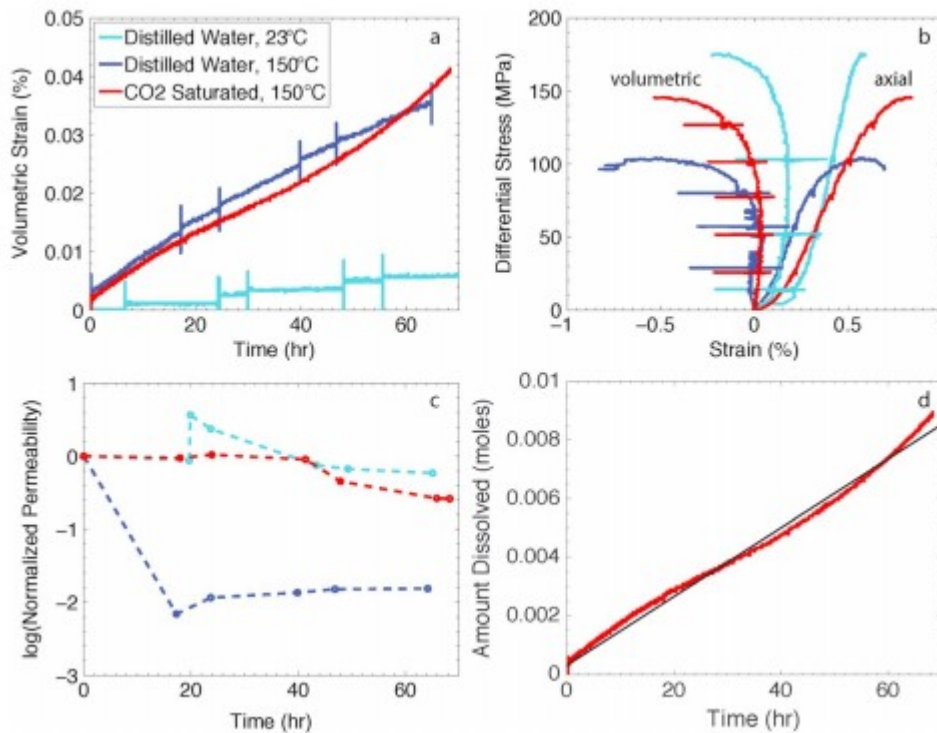


Figure 1

Mechanical and permeability data from experiments. (a) Volumetric strain versus time for hydrostatic creep experiments. Compactive strain is designated to be positive. The red curve is the data from the sample saturated with $CO_2$-rich bicarbonate solution at 150°C, the dark blue curve is the data from the sample saturated with distilled water at 150°C, and the cyan curve is the data from the sample saturated with distilled water at 23°C. (b) Stress-strain curves for constant strain rate deformations after 3 days reaction. Color is the same as in Figure 1a. The sample saturated with $CO_2$-rich bicarbonate solution shows enhanced compaction compared to the sample saturated with distilled water. (c) Normalized permeability versus time. Color is the same as above. Sample saturated with distilled water shows enhanced permeability reduction compared to the sample saturated with $CO_2$ brine. (d) Calculated moles dissolved versus time for $CO_2$-rich bicarbonate solution, from which effective reaction rate was calculated. The red line is the data, and the black line is a linear fit to the data.

## 3.2 Microstructures

Microstructural observation of the samples after experiments shows that the chemo-mechanical coupling is caused by interplay of dissolution and precipitation processes at fluid-rock interfaces. SEM images of polished thin sections of the experimental samples (Figures 2a and 2b) show that the initial sample material is largely monomineralic olivine with trace chromite,

and pore space consists of almost entirely high-aspect ratio thermal cracks. Mechanically induced cracks and chemically induced secondary porosity are easily distinguished in reacted samples by morphology and the absence of precipitates in the former. Since the axial deformation portions of experiments were short (<2 h), nearly all of the precipitation occurs during the longer hydrostatic stage. Due to the low oxygen and water fugacities during the thermal cracking process, samples are initially serpentine free. Initially, crack surfaces are clean and edges angular (supporting information Figure S3a), while after reaction, crack surfaces are covered in precipitation (supporting informationFigure S3b). The sample reacted with distilled water at room temperature shows slight rounding of angular edges, but surfaces remain clean (supporting information Figure S3c). The distilled water sample at 150°C shows more pronounced rounding of angular edges and secondary serpentine (supporting information Figure S3d). One pervasive feature in samples reacted with $CO_2$-rich solutions is the presence of dissolution channels initiated at primary crack surfaces (Figures 2b–2d). The seeming coalescence of these channels to form a region of high porosity at ~10 μm in primary crack surfaces is particularly striking (Figures 2d and 2f). To investigate this structure with greater detail than was possible with polished thin sections, unpolished samples were broken open along preexisting primary cracks and the surfaces of those cracks analyzed. The topography of the unpolished surfaces rendered quantitative chemical analysis difficult, but coupling qualitative EDS with observations of well-terminated crystal habits led to greater confidence in mineral identification.
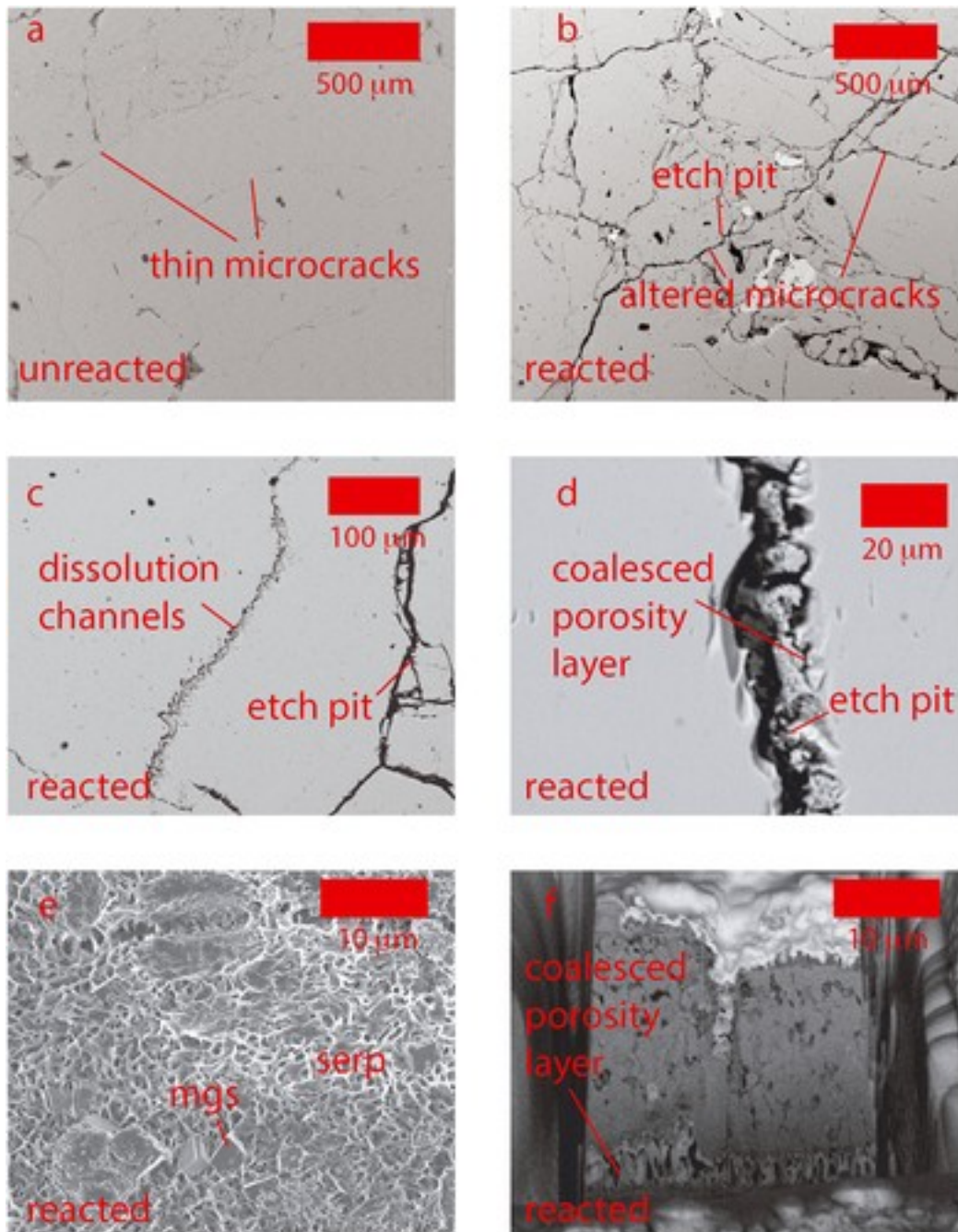
Figure 2

SEM images from experimental samples showing pervasive dissolution features along cracks. (a) Unreacted sample shows thin microcracks and no dissolution features. (b) Reacted sample shows wider cracks with pitted margins. (c) Dissolution channels form inward from primary crack surfaces. (d) Dissolution channels coalesce at some distance from the primary cracks, providing additional fluid pathways while primary porosity is filled with secondary minerals. (e) View of unpolished crack surface showing pervasive precipitation of magnesite, serpentine, and amorphous phases. (f) Face of FIB section into crack surface showing dissolution channels and coalesced porosity band.

The microstructure of the sample with distilled water at 150°C suggests transport-controlled dissolution (Lasaga & Kirkpatrick, 1981). Crack surfaces are smooth and show slight secondary mineralization of a platy mineral

(supporting information Figure S3d), which EDS analysis indicates has the composition of serpentine, as well as some material with no discernable crystal habit, and a slight silica enrichment, suggesting amorphous silica on top of olivine or so-called "amorphous protoserpentine" (i.e., Plumper et al., 2012). In comparison, the sample with $CO_2$-rich bicarbonate solution as pore fluid shows more prominent alteration. Surfaces exhibit substantial pitting (i.e., Figures 2b–2f), indicating relatively rapid, reaction-controlled dissolution (Lasaga & Kirkpatrick, 1981). Secondary mineralization is ubiquitous, with crack surfaces supporting intergrown patches of amorphous material, serpentine, magnesite, and hydrated magnesium carbonate (perhaps hydromagnesite or nesquehonite, based on crystal habit) (Figure 2e). The secondary mineralization is highly porous, some of the most striking features of these samples are the deep, interconnected etch pits, some of which resemble wormholes (e.g., Ott & Oedai, 2015).

## 3.3 Three-Dimensional Image Analysis

To investigate the 3-D structure of the etch pits, several serial FIB-SEM sections were cut into the crack surface. FIB data were analyzed in 3-D using several open source and commercial software packages. Image slices are first filtered to reduce noise using an edge-preserving, anisotropic diffusion filter then registered to reduced image translation due to FIB beam shifts using the open software package ImageJ. The stacked data are then converted and imported into the commercial software package Avizo where they are segmented using threshold segmentation into pore space and solid mineral.

Analysis of the data from FIB-SEM sections of samples reacted with $CO_2$-rich solutions shows the presence of a band of enhanced porosity parallel to and 8–10 µm beneath crack surfaces (Figure 3). Dissolution is channelized and heterogeneous. Secondary porosity is quasi-spherical and/or quasi-cylindrical and is geometrically distinct from the high-aspect ratio thermal cracks that make up the primary porosity. Unreacted samples do not exhibit this feature (supporting information Figure S4). Induced porosity, here taken to be any porosity other than primary grain boundary cracks, ranges from 20 to 60% within the highly porous band. Image analysis indicates that the secondary porosity is interconnected and exhibits anisotropic permeability.
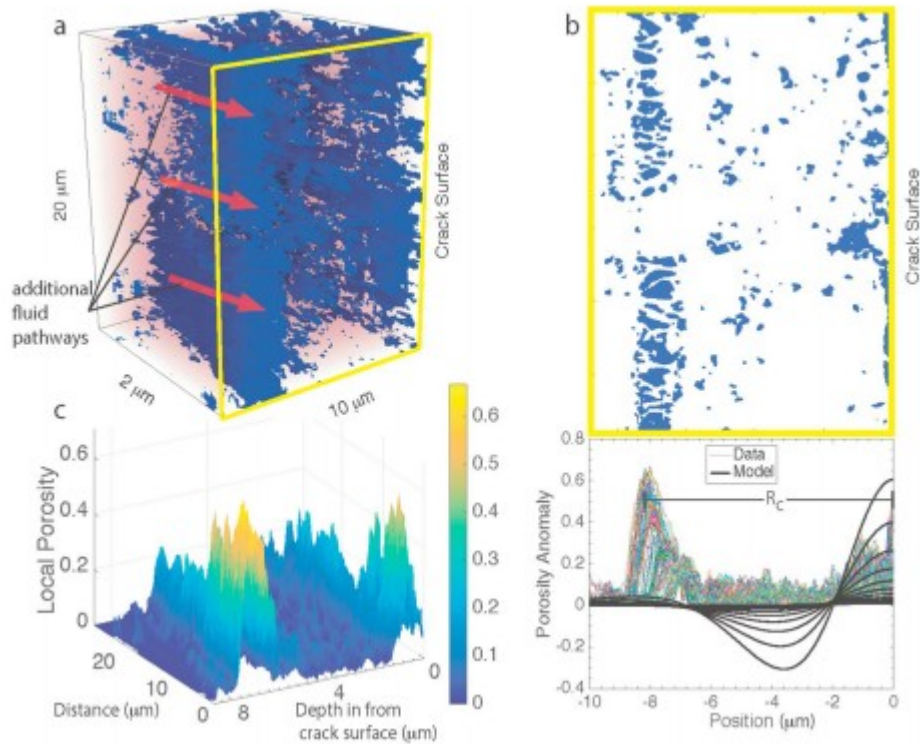
Figure 3

Data from FIB serial section of altered dunite. (a) Volumetric reconstruction of pore space imaged by FIB-SEM shows concentrated band of porosity ~8 μm down from the crack surface. (b) Top panel shows binarization of one slice of FIB data, with porosity in blue. Bottom panel shows average porosity along all slices in thin-colored lines and model results in black bold lines, with lines representing successive time steps [25]. Spacing of porosity bands, $R_c$, agrees with model of induced porosity. (c) Image analysis shows that local porosity in the band varies from ~20 to 60%. Colors correspond to local porosity values calculated as the ratio of pore space to solid along a line.

The pore space is meshed and used as the flow geometry for a permeability tensor simulation with the result:

$$K = \begin{vmatrix} 0 & 0 & 0 \\ 0 & 0 & 0 \\ 0 & 0 & 8\times10^{-18}\ m^2 \end{vmatrix}$$

with the *z* direction parallel to the original crack surface. The volume analyzed is not representative of the entire sample, so these data are difficult to interpret beyond the observation that there is a particular direction of preferred flow, possibly related to the crystallographic orientation of the dissolving grain.

We conducted a complimentary X-ray nano-CT scan on olivine grains that have undergone 5 days of carbonation reaction at a confining pressure of 13 MPa, pore pressure of 10 MPa, and temperature of 200°C (see Zhu et al., 2016 for details of the reactive experiment). The nano-CT was conducted using a transmission X-ray microscope with an 8 keV X-ray monochromatic

beam at the beamline 32-ID of the Advanced Photon Source of Argonne National Laboratory (De Andrade et al., 2016). An X-ray objective lens corresponding to a Fresnel zone plate with 60 nm outermost zone width was used to magnify radiographs onto a detection system assembly comprising a scintillator (LuAG), a Zeiss 5X optical microscope objective lens, and an Andor Neo sCMOS camera. The Fresnel zone plate limits the spatial resolution to 60 nm, while the voxel size is 57 nm after binning. Total 720 projection images were acquired in 180° rotation angle range (i.e., 0.25° per angular step) with 2 s exposure time for each image. Three-dimensional reconstructions were performed with Tomopy, an open source collaborative framework for the analysis of synchrotron tomographic data (De Carlo et al., 2014; Gürsoy et al., 2014; Pelt & Batenburg, 2015) using the generalized Titarenko's algorithm for ring removal (Miqueles et al., 2014). Movie S1 is a 3-D rendering visualization proposing a walk through the reconstructed slices, highlighting the segmentation of the wormhole shape porosity inside olivine grains.

## 4 Discussion

### 4.1 Mechanical Behavior

At 150°C, the sample with distilled water compacts with a monotonically decreasing rate during hydrostatic loading (blue curve, Figure 1a), which is consistent with dissolution-assisted closure of preexisting cracks. Dissolution can be rigorous at contacting asperities with high concentrated stress, resulting in relatively high initial compaction rates. As the asperities are dissolved, asperities flatten, the local stress decreases, and thus dissolution-assisted compaction slows down. The dissolution of asperities is also inferred to occur in the sample with $CO_2$-rich bicarbonate solution, but the presence of $CO_2$ results in precipitation of carbonate minerals, increasing solid volume and competing with dissolution-assisted compaction. Triaxial compression tests indicate that the sample with distilled water has lower yield strength and more dilatancy after reaction than the sample with $CO_2$-rich bicarbonate solution (Figure 1b).

Assuming that all of the sample compaction is the result of olivine dissolution (Figure 1d) and using a typical-specific surface area for thermally cracked crystalline rocks of 3 $m^{-1}$(Darot et al., 1992), an effective dissolution rate of $10^{-12}$ $mol/cm^2$ s is obtained, a number that is generally consistent with rates obtained from experiments on olivine powders at similar pH and temperature conditions (Hänchen et al., 2006). This is somewhat surprising given that rates measured from powders are typically faster than for aggregate samples and our calculated rate can be regarded as a low bound; however, our estimate of specific surface area used in the calculation does not account for additional surface area introduced due to channelized dissolution. Previous studies have suggested that grain boundary structure may control effective olivine dissolution rate (van Noort et al., 2013). Microstructural analysis of our samples after reaction indicates a positive feedback between

dissolution and grain boundary structure that may provide a mechanism for maintaining porosity.

## 4.2 Porosity Band Model

A model from Merino et al. (1983) was used to reproduce the experimentally observed dissolution patterns. This model couples stress-dependent dissolution with diffusion of dissolved species through stagnant fluid using the equations

$$\frac{\partial \psi}{\partial \bar{t}} = -\left(1 - \bar{\phi}\psi\right)^{2/3}\left[\sigma - \sigma^{eq}(\psi)\right]$$ (3)

$$B\psi \frac{\partial \sigma}{\partial \bar{t}} = \frac{\partial}{\partial \bar{s}}\left(\psi^m \frac{\partial \sigma}{\partial \bar{s}}\right) - \left(1 - \bar{\phi}\psi\right)^{2/3}\left[\sigma - \sigma^{eq}(\psi)\right]\cdot\left[1 - \varepsilon e^\lambda(1 + \omega\sigma)\right]$$ (4)

where $\psi$ is the porosity anomaly or deviation from average porosity,  is dimensionless time, is average porosity, $\sigma$ is a measure of the chemical potential, $\sigma^{eq}(\psi)$ is a function describing the porosity dependence of chemical potential, B is a constant,  is dimensionless space, $m$ is a power law constant, $\varepsilon$ is the ratio of dissolved molar component to the solid molar volume, $\lambda$ is a constant related to the stress dependence of chemical potential, and $\omega$ is related to the total chemical potential of the system. For details of the model, see Merino et al. (1983). These equations are solved using the MATLAB stiff solver ode15s, using the initial one-dimensional geometry of a small positive porosity anomaly representing a crack in an otherwise solid rock. The model shows that this porosity anomaly grows and also induces a satellite band of porosity some distance from the initial crack. The model also predicts that such satellite porosity bands will form at a characteristic distance, $R_c$,

$$R_c = \left(D_c \bar{\phi}^m / k n^{1/3}\right)^{1/2}$$ (5)

where $D_c$ is the diffusion constant, $k$ is reaction rate, and $n$ is the pore geometry parameter. Using the parameter values appropriate for our experimental conditions, we get a value of 8.3 µm, in very good agreement with the observed 8 µm spacing of our secondary porosity, though this value should not be overinterpreted as the calculation is meant only to yield order of magnitude estimates. Parameters used in this calculation are presented in supporting information Table S1.

## 4.3 Mechanism of Porosity Organization

The proposed mechanism for generating such secondary porosity is presented in Figure 4. Etch pit nucleation in olivine commonly begins at local chemical potential maxima caused by stress associated with near-surface dislocations (Dove et al., 2005). These etch pits are stress risers that promote dissolution (Kamb, 1959), which results in a reactive instability and growth of quasi-cylindrical pores. Our experiments had static pore fluid; thus,

dissolved species transport is controlled mainly by diffusion. The diffusion referred to here is the mechanism by which dissolved species move within the pore fluid, in contrast to advection. The difference between transport and reaction-controlled cases is the relative rates of reaction and transport. In these experiments where little advection is taking place within the pore space, the transport mechanism is diffusion. The difference in microstructure between the samples reacted with distilled water and those reacted with $CO_2$-rich solution is the result of the mechanism we detail in Figure 4. Absent the constant removal of Mg from solution by carbonate precipitation, the dissolution of olivine is relatively slowed in the distilled water experiment, leading to a lack of extensive dissolution channeling.
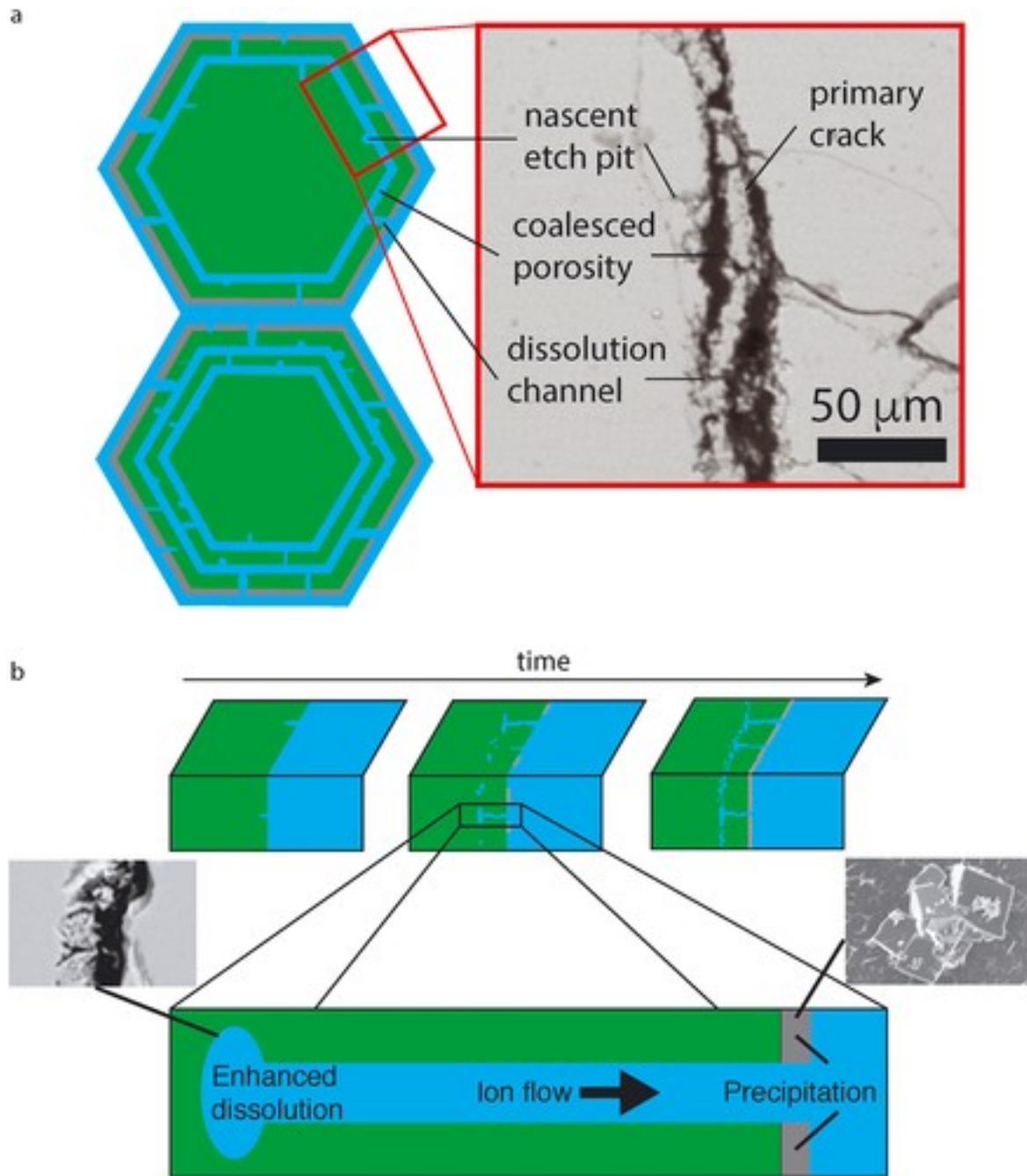
Figure 4

Conceptual model of locally enhanced compressive stress-induced porosity bands. (a) Inward growth of porosity bands causes radially inward alteration. Green represents olivine, blue represents pore fluid, and grey represents precipitation. Dissolution divides olivine grains into small domains with enhanced reactive surface area. (b) Concentration gradient between zone of enhanced porosity and primary pore space leads to preferential flow of dissolved species, leading to positive feedback.

The coupling of this enhanced dissolution and diffusion can induce satellite porosity bands with characteristic spacing (Merino et al., 1983). Using the model from Merino et al. (1983) with parameters corresponding to our experimental conditions (see supporting informationTable S1), we can

reproduce the 8 µm spacing; however, the model underpredicts the magnitude of porosity change. The model assumes a monomineralic system with a single dissolved species and a simple one-dimensional geometry, deviations from which may explain these discrepancies. In a monomineralic system, chemical potential differences are driven only by stress; in our experiments, the pore fluid is initially undersaturated with olivine, and precipitation of secondary minerals constantly removes dissolved species from solution, causing their depletion and driving dissolution.

Most secondary mineralization is observed along preexisting crack surfaces rather than within small secondary pores (Figure 2). The high curvature of the small pores suppresses precipitation (Putnis & Mauthe, 2001), leading to elevated concentrations of dissolved species in these pores compared to the bulk fluid, in which the concentrations of dissolved species are buffered by secondary mineralization. This results in a concentration gradient between the secondary pores and the primary pores, i.e., preexisting cracks, which leads to a dynamic flow of dissolved species. This flow coupled with the stress-dependent growth of localized secondary porosity provides a mechanism for local intensification of deformation, while precipitation of secondary minerals along crack surfaces can laterally inhibit dissolution and deformation. The result is a pattern of locally intensified compressional stress-induced porosity bands (Figure 4).

This conceptual model is consistent with the interface-coupled dissolution-precipitation reactions understood to mediate phase transitions in many aqueous systems (Putnis & Putnis, 2007). In such reactions, reactive surface area is maintained by an asymmetry in dissolution and precipitation caused by the relative thermodynamic stability of the secondary minerals as compared to dissolving phase. During the olivine carbonation reaction, the rapid dissolution rate of olivine is coupled with the slower precipitation of magnesium carbonate (Xu et al., 2013). The asymmetry is so great that channelized olivine dissolution can separate olivine grains into domains which are subsequently exposed on all sides to reactive fluid, eventually leading to a layered structure (Figure 4a). Similar structures to those observed in our experiments have been observed in the replacement of KBr with K(Br,Cl) as documented by Raufaste et al. (2010). In that system, the products of the reaction have a smaller volume than the reactants and therefore pore space is generated. The resultant pore channels are homogeneous on a sample scale. In our experiments, the dissolution channels proceed only into olivine as measured by EDS and the products of the reaction precipitate outside the dissolution channel network. The transport of the dissolved olivine out of the secondary porosity is essentially what causes the formation of the satellite porosity band as predicted by the model (Merino et al., 1983). It is also possible that the rapid reaction and short duration of the experiments performed by Raufaste et al. (2010) do not allow sufficient time for transport of dissolved species out of the secondary pore network.

The preexisting thermal cracks, which augment the reaction rate in our experiments, are not required for dissolution channel formation. In experiments on olivine aggregates with smaller grain sizes, X-ray nano-Computed Tomography (nano-CT) shows that these dissolution channels entirely bifurcate grains in a process similar to dissolution-facilitated subcritical crack growth, which may provide a mechanism for the production of hierarchical crack networks to form under a subcritical stress state (see supporting information Movie S1). This subcritical crack growth mechanism is commonly understood to control joint sets (Savalli & Engelder, 2005) with similar structural characteristics as observed in altered ultramafic rocks (Plumper et al., 2012).

5 Conclusions

In nature, hydrothermally altered ultramafic rocks often exhibit structures suggesting self-organized fracture networks that appear to be controlled by interaction of chemical and physical stresses. Our experiments under controlled conditions demonstrate growth of secondary porosity during olivine carbonation amid dissolution and precipitation of secondary minerals. The microstructural evidence supports a mechanism that explains commonly observed structures through the formation of locally intensified compressional stress-induced porosity bands and the propagation of dissolution-assisted subcritical cracks. This type of deformation does not require a large force of crystallization to be exerted by the growth of secondary minerals in a confined pore space, allowing for the slow growth of fracture networks at subcritical stress intensities.

References

Andreani, M., Luquot, L., Gouze, P., Godard, M., Hoisé, E., & Gibert, B. (2009). Experimental study of carbon sequestration reactions controlled by the percolation of $CO_2$-rich brine through peridotites. *Environmental Science & Technology*, 43, 1226– 1231.

Andreani, M., Mével, C., Boullier, A.-M., & Escartín, J. (2007). Dynamic control on serpentine crystallization in veins: Constraints on hydration processes in oceanic peridotites. *Geochemistry, Geophysics, Geosystems*, 8, Q02012. https://doi.org/10.1029/2006GC001373

Beinlich, A., Plümper, O., Hövelmann, J., Austrheim, H., & Jamtveit, B. (2012). Massive serpentinite carbonation at Linnajavri, N-Norway. *Terra Nova*, 24, 446– 455.

Boitnott, G. N. (1997), Use of complex pore pressure transients to measure permeability of rocks. SPE Annual Technical Conference and Exhibition. Houston, TX: Society of Petroleum Engineers.

Darot, M., Gueguen, Y., & Baratin, M. (1992). Permeability of thermally cracked granite. *Geophysical Research Letters*, 19, 869– 872. https://doi.org/10.1029/92GL00579

De Andrade, V., A. Deriy, M. J. Wojcik, D. Gürsoy, D. Shu, K. Fezzaa and F. De Carlo (2016), Nanoscale 3D imaging at the advanced photon source, SPIE newsroom, 12 May. https://doi.org/10.1117/2.1201604.006461

De Carlo, F., Gursoy, D., Marone, F., Rivers, M., Parkinson, Y. D., Khan, F., … Jacobsen, C. (2014). Scientific data exchange: A schema for hdf5-based storage of raw and analyzed data. *Journal of Synchrotron Radiation*, 21( 6), 1224– 1230.

Deschamps, F., Godard, M., Guillot, S., & Hattori, K. (2013). Geochemistry of subduction zone serpentinites: A review. *Lithos*, 178, 96– 127.

Dove, P. M., Han, N., & De Yoreo, J. J. (2005). Mechanisms of classical crystal growth theory explain quartz and silicate dissolution behavior. *Proceedings of the National Academy of Sciences of the United States of America*, 102, 15,357– 15,362.

Escartin, J., Hirth, G., & Evans, B. (1997). Nondilatant brittle deformation of serpentinites: Implications for Mohr-Coulomb theory and the strength of faults. *Journal of Geophysical Research*, 102, 2897– 2913.

Falk, E. S., & Kelemen, P. B. (2015). Geochemistry and petrology of listvenite in the Samail ophiolite, Sultanate of Oman: Complete carbonation of peridotite during ophiolite emplacement. *Geochimica et Cosmochimica Acta*, 160, 70– 90.

Gürsoy, D., De Carlo, F., Xiao, X., & Jacobsen, C. (2014). TomoPy: A framework for the analysis of synchrotron tomographic data. *Journal of Synchrotron Radiation*, 21, 1188– 1193.

Hänchen, M., Prigiobbe, V., Storti, G., Seward, T. M., & Mazzotti, M. (2006). Dissolution kinetics of fosteritic olivine at 90–150°C including effects of the presence of CO2. *Geochimica et Cosmochimica Acta*, 70, 4403– 4416.

Hövelmann, J., Austrheim, H., & Jamtveit, B. (2012). Microstructure and porosity evolution during experimental carbonation of a natural peridotite.

*Chemical Geology*, 334, 254– 265. https://doi.org/10.1016/j.chemgeo.2012.10.025

Iyer, K., Jamtveit, B., Mathiesen, J., Malthe-Sørenssen, A., & Feder, J. (2008). Reaction-assisted hierarchical fracturing during serpentinization. *Earth and Planetary Science Letters*, 267, 503– 516.

Jamtveit, B., & Hammer, Ø. (2012). Sculpting of rocks by reactive fluids. *Geochemistry Perspectives*, 1, 341– 481.

Jamtveit, B., Malthesorenssen, A., & Kostenko, O. (2008). Reaction enhanced permeability during retrogressive metamorphism. *Earth and Planetary Science Letters*, 267( 3–4), 620– 627.

Johnson, J. W., Oelkers, E. H., & Helgeson, H. C. (1992). SUPCRT92: A software package for calculating the standard molal thermodynamic properties of minerals, gases, aqueous species, and reactions from 1 to 5000 bar and 0 to 1000 C. *Computers & Geosciences*, 18, 899– 947.

Kamb, W. B. (1959). Theory of preferred crystal orientation developed by crystallization under stress. *Journal of Geology*, 67, 153– 170.

Kelemen, P. B., & Hirth, G. (2012). Reaction-driven cracking during retrograde metamorphism: Olivine hydration and carbonation. *Earth and Planetary Science Letters*, 345, 81– 89.

Kelemen, P. B., & Matter, J. (2008). In situ carbonation of peridotite for $CO_2$ storage. *Proceedings National Academy Science U.S.A.*, 105, 17,295– 17,300.

Kelley, D. S., Karson, J. A., Früh-Green, G. L., Yoerger, D. R., Shank, T. M., Butterfield, D. A., … Jakuba, M. (2005). A serpentinite-hosted ecosystem: The lost city hydrothermal field. *Science*, 307, 1428– 1434.

Lasaga, A. C., & Kirkpatrick, R. J. (1981). Kinetics of geochemical processes. *Reviews in Mineralogy*, 3.

Lisabeth, H. P., Zhu, W., Kelemen, P. B., & Ilgen, A. (2017). Experimental evidence for chemo-mechanical coupling during carbon mineralization in ultramafic rocks. *Earth and Planetary Science Letters*, 474, 355– 367.

Merino, E., Ortoleva, P., & Strickholm, P. (1983). Generation of evenly-spaced pressure-solution seams during (late) diagenesis: A kinetic theory. *Contributions to Mineralogy and Petrology*, 82, 360– 370.

Miqueles, E. X., Rinkel, J., O'Dowd, F., & Bermúdez, J. S. V. (2014). Generalized Titarenko's algorithm for ring artefacts reduction. *Journal of Synchrotron Radiation*, 21( 6), 1333– 1346.

Ott, H., & Oedai, S. (2015). Wormhole formation and compact dissolution in single-and two-phase $CO_2$-brine injection. *Geophysical Research Letters*, 42, 2270– 2276. https://doi.org/10.1002/2015GL063582

Pelt, D. M., & Batenburg, K. J. (2015), Accurately approximating algebraic tomographic reconstruction by filtered backprojection. In proceedings of the

2015 international meeting on fully three-dimensional image reconstruction in radiology and nuclear medicine.

Plumper, O., Royne, A., Magraso, A., & Jamtveit, B. (2012). The interface-scale mechanism of reaction-induced fracturing during serpentinization. *Geology*, 40, 1103– 1106.

Putnis, A., & Mauthe, G. (2001). The effect of pore size on cementation in porous rocks. *Geofluids*, 1, 37– 41.

Putnis, A., & Putnis, C. V. (2007). The mechanism of reequilibration of solids in the presence of a fluid phase. *Journal of Solid State Chemistry*, 180, 1783– 1786.

Raufaste, C., Jamtveit, B., John, T., Meakin, P., & Dysthe, D. K. (2010). The mechanism of porosity formation during solvent-mediated phase transformations. *Proceedings of the Royal Society of London Series A*, 22, 1408– 1426.

Røyne, A., Jamtveit, B., Mathiesen, J., & Malthe-Sørenssen, A. (2008). Controls on rock weathering rates by reaction-induced hierarchical fracturing. *Earth and Planetary Science Letters*, 275, 364– 369.

Rumori, C., Mellini, M., & Viti, C. (2004). Oriented, non-topotactic olivine → serpentine replacement in mesh-textured, serpentinized peridotites. *European Journal of Mineralogy*, 16, 731– 741.

Savalli, L., & Engelder, T. (2005). Mechanisms controlling rupture shape during subcritical growth of joints in layered rocks. *Geological Society of America Bulletin*, 117, 436– 449.

Scherer, G. W. (2004). Stress from crystallization of salt. *Cement and Concrete Research*, 34, 1613– 1624.

Seifritz, W. (1990). $CO_2$ disposal by means of silicates. *Nature*, 345, 486.

van Noort, R., Spiers, C. J., Drury, M. R., & Kandianis, M. T. (2013). Peridotite dissolution and carbonation rates at fracture surfaces under conditions relevant for in situ mineralization of $CO_2$. *Geochimica et Cosmochimica Acta*, 106, 1– 24.

Watson, E. B. (1991). Diffusion in fluid-bearing and slightly-melted rocks: Experimental and numerical approaches illustrated by iron transport in dunite. *Contributions to Mineralogy and Petrology*, 107( 4), 417– 434.

Wolterbeek, T. K., Hangx, S. J., & Spiers, C. J. (2016). Effect of $CO_2$-induced reactions on the mechanical behaviour of fractured wellbore cement. *Geomechanics for Energy and the Environment*, 7, 26– 46.

Xu, J., Yan, C., Zhang, F., Konishi, H., Xu, H., & Teng, H. (2013). Testing the cation-hydration effect on the crystallization of Ca–Mg–$CO_3$ systems. *Proceedings of the National Academy of Sciences of the United States of America*, 110, 17,750– 17,755.

Zhu, W., Fusseis, F., Lisabeth, H., Xing, T., Xiao, X., De Adndrade, V., & Karato, S. I. (2016). Experimental evidence of reaction-induced fracturing during olivine carbonation. *Geophysical Research Letters*, 43, 9535– 9543. https://doi.org/10.1002/2016GL070834